

Inhomogeneous Perpendicular Magnetic Anisotropy as a Source of Higher-order Quasistatic and Dynamic Anisotropies

J. B. Mohammadi – The University of Alabama

K. Cole – The University of Alabama

T. Mewes – The University of Alabama

C. K. A. Mewes – The University of Alabama

Deposited 08/30/2018

Citation of published version:

Mohammadi, J., Cole, K., Mewes, T., Mewes, C. (2018): Inhomogeneous Perpendicular Magnetic Anisotropy as a Source of Higher-order Quasistatic and Dynamic Anisotropies, *Physical Review B* 97.

<https://doi.org/10.1103/PhysRevB.97.014434>

Inhomogeneous perpendicular magnetic anisotropy as a source of higher-order quasistatic and dynamic anisotropies

J. B. Mohammadi, K. Cole, T. Mewes, and C. K. A. Mewes

Department of Physics and Astronomy, MINT Center, The University of Alabama, Tuscaloosa, Alabama 35487, USA

 (Received 11 September 2017; revised manuscript received 8 November 2017; published 26 January 2018)

We investigate the influence of lateral variations of the second-order perpendicular anisotropy in thin films on the effective anisotropies required to represent this structure using a macrospin approximation. Second-order and fourth-order effective anisotropies are required for the macrospin approximation. In the case of quasistatic calculations, the fourth-order effective anisotropy is closely linked to deviations of the average magnetization angle from the field direction and lateral variations of the magnetization direction in the structure leading to dependence on the field strength and the lateral length scale of anisotropy variations of the effective anisotropies. We find that the field and lateral length-scale dependence of the effective anisotropies extracted from simulations of the magnetization dynamics are profoundly different from those of the quasistatic simulations. This is caused by resonance localization that depends on the orientation of the external magnetic field.

DOI: [10.1103/PhysRevB.97.014434](https://doi.org/10.1103/PhysRevB.97.014434)

I. INTRODUCTION

The presence of a strong perpendicular anisotropy is of significant importance for materials intended for use in spintronic devices. For example, a significant reduction of the switching current density while maintaining the thermal stability for spin transfer torque magnetic random-access memories (STT-MRAM) can be achieved by utilizing a perpendicular anisotropy [1,2]. One common observation in these materials is that in order to accurately describe their quasistatic or dynamic properties one has to include both second-order (K_2) and fourth-order uniaxial anisotropy (K_4) contributions to the anisotropy energy density E_{aniso} [3–7]:

$$E_{\text{aniso}} = K_2 \cos^2 \theta_M + \frac{K_4}{2} \cos^4 \theta_M, \quad (1)$$

where θ_M is the angle of the magnetization with respect to the film normal. We note that the nomenclature for the anisotropy constants is inconsistent in the literature, as they are also referred to as first-order and second-order anisotropy constants. With the above definition, the film normal is an easy axis of the corresponding anisotropy contribution for $K_i < 0$, but the opposite sign convention is also commonly used in the literature.

By using a second-order perturbation of the tight binding model, Bruno was able to show the connection of the asymmetry in the orbital moment and the second-order anisotropy K_2 [8]. However, currently, a clear theoretical picture for the origin of the fourth-order anisotropy K_4 is lacking. While recent fully relativistic *ab initio* calculations have shown the presence of such a term, its magnitude was only 3% of the second-order anisotropy [9]. Recently, the possibility of macroscopic anisotropies induced by the Dzyaloshinsky-Moriya interaction (DMI) [10,11] has regained interest [12], but we are currently not aware of work investigating the possibility of DMI induced higher-order anisotropies.

However, using analytical models it has been shown that lateral fluctuations of the second-order perpendicular anisotropy can lead to the emergence of higher-order anisotropy terms

[13,14]. Here, we report on detailed micromagnetic [15–19] investigations of lateral variations of the second-order perpendicular anisotropy and its influence on the magnetization dynamics and the quasistatic properties of thin films. We analyze these micromagnetic simulations, by determining the parameters that best describe the results using a macrospin model, i.e., a model that represents the entire system as a single macrospin with effective anisotropies. This is a common approach [20–24] and has the advantage that it closely resembles the way the experimental data of these systems are typically analyzed. We show that in order to achieve a good macrospin description of the micromagnetic simulations, a fourth-order uniaxial anisotropy contribution is required, although the micromagnetic model does not include such a term.

The manuscript is structured as follows. First, we start with a description of the theoretical background and explanation of the methodology relevant for the micromagnetic calculations and their analysis in the framework of the macrospin model. In the next section, we discuss the quasistatic properties of the system, starting with a detailed discussion of the angular dependence of the different contributions to the energy of the system and how they contribute to the effective anisotropies that are required when representing the system with a macrospin model. We also investigate the field dependence of the effective anisotropies [25]. In the subsequent section, we discuss the influence of the length scale of the lateral variations of the second-order anisotropy on the effective anisotropies. After this, we analyze the dynamic properties of the system and compare their dependence on the length scale of the lateral variations of the second-order uniaxial anisotropy with those of the quasistatic properties. We conclude with a summary and discussion of our results.

II. RESULTS AND DISCUSSION

A. Theoretical background (methodology)

A common approach when trying to describe the quasistatic and dynamic properties of a complex magnetic system is to

utilize the so-called macrospin model, which does not take into account the spatial variations of the magnetization in the system. Even for systems that are known to have spatial variations, the macrospin model is often used to analyze experimental data. To investigate the influence of spatial variations of the second-order uniaxial anisotropy on the magnetic properties we model the system micromagnetically [15–19]. We then determine the parameters of the macrospin model that best describe the micromagnetic results. In Secs. II B and II C we focus on the quasistatic properties of the system that are obtained after the system has relaxed to equilibrium, whereas Sec. II D focusses on the dynamic properties, that are obtained by analyzing the time dependence of the magnetization.

For the micromagnetic modeling we use our finite differences code M^3 [26] written in the MATLAB scripting language. M^3 uses a fast Fourier transform (FFT) method to calculate the magnetostatic interactions. M^3 utilizes Newell’s formulation to calculate the demagnetizing tensor at short distances [27] and a dipole approximation for the far field. For the current work, we used the six-neighbor method for the exchange interaction and Neuman boundary conditions [28].

For the simulations, the perpendicular magnetic anisotropy is assumed to be constant across the film thickness, i.e., in our model we use the thickness-averaged perpendicular anisotropy. However, the model takes into account lateral variations of this thickness-averaged perpendicular anisotropy, which could, for example, be caused by lateral variations of the strength of the interfacial perpendicular anisotropy or by lateral variations of the film thickness. Instead of attempting to model a specific system, for which one would have to make assumptions about the details of the interfacial roughness and its influence on the length scale and amplitude of the lateral variations of the perpendicular anisotropy, our aim is to capture the basic physics by using a simplified model.

Our model incorporates lateral variations of the second-order uniaxial anisotropy in the form of a periodic checkerboard structure, as pictured in Fig. 1. For all simulations regions A have a second-order perpendicular anisotropy, $K_{2,A} = -1.5 \times 10^6 \text{ J/m}^3$, which is sufficient to overcome the demagnetizing field and thus results in an easy axis of these regions along the film normal. While the strength of the second-order perpendicular anisotropy $K_{2,B} \geq 0$ of regions B was varied for different simulations, the film normal for these regions is always a hard axis. In the micromagnetic simulations, both regions have no intrinsic fourth-order uniaxial anisotropy, i.e., $K_{4,A} = K_{4,B} = 0$. However, as will be shown below, the frustration between these two regions caused by their different second-order uniaxial anisotropies leads to the emergence of a fourth-order anisotropy contribution of the system when analyzed in the macrospin approximation. For the saturation magnetization of the system we chose $M_S = 1000 \text{ kA/m}$, while the exchange constant was set to $A = 1 \times 10^{-11} \text{ J/m}$. The wavelength $L_{x,y}$ of the pattern was chosen to be the same along both in-plane directions and for the following discussion was set to $L_x = L_y = 30 \text{ nm}$, the cell size was $1 \text{ nm} \times 1 \text{ nm} \times 1 \text{ nm}$. The influence of the length scale of the lateral anisotropy variations is investigated in detail in Sec. II C.

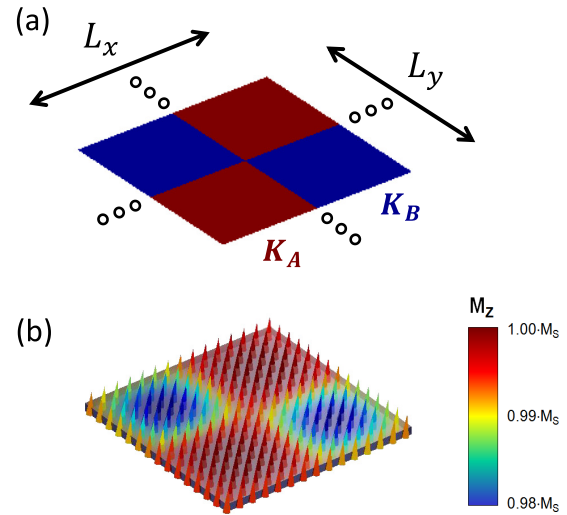


FIG. 1. (a) Periodic checkerboard pattern used for the simulations, regions A have a second-order perpendicular anisotropy $K_{2,A} = -1.5 \times 10^6 \text{ J/m}^3$ whereas for regions B $K_{2,B} \geq 0$. (b) Relaxed magnetization with an external magnetic field of $\mu_0 H = 1 \text{ T}$ applied at an angle of $\theta_H = 5^\circ$ with respect to the film normal.

B. Magnetic field dependence of the quasistatic properties

To determine the quasistatic properties of the system, an external magnetic field \vec{H} is applied at different angles θ_H with respect to the film normal. After relaxing the system, the magnetization will locally be aligned with the effective field, i.e., the sum of all internal fields. Overall, the magnetization appears to be mostly aligned along the direction of the strong external magnetic field. However, a close inspection shows that the degree of alignment differs in the two regions, as shown in Fig. 1(b). To quantitatively analyze these simulations, we calculate the average angle of the magnetization $\theta_M = \frac{1}{N} \sum_i \theta_{M,i}$ with respect to the film normal and the different contributions to the total energy density of the relaxed structure averaged over all N cells in the simulation volume. The micromagnetic simulations enable the determination of the different contributions to total energy density E_{total} of the system [15–19,26]. This includes the demagnetizing energy E_{demag} caused by the dipole-dipole interaction between the magnetic cells in the simulation volume [27]. In addition, the orientation of the magnetization in each cell with respect to the film normal will lead to an energy density contribution $E_{\text{anisotropy}}$ due to the local anisotropy described by Eq. (1). Furthermore, the orientation of the magnetization in each cell with respect to the external magnetic field leads to a spatially varying Zeeman energy density contribution E_{Zeeman} [29]. Finally, the exchange interaction [29] leads to an exchange energy density contribution E_{exchange} that depends on the misalignment of the magnetizations in neighboring cells [28]:

$$E_{\text{total}} = E_{\text{demag}} + E_{\text{anisotropy}} + E_{\text{Zeeman}} + E_{\text{exchange}}. \quad (2)$$

The micromagnetic model enables us to determine all energy contributions independently after the system has relaxed to its equilibrium.

In Fig. 2, the total energy density and the individual contributions are shown as a function of the average angle of

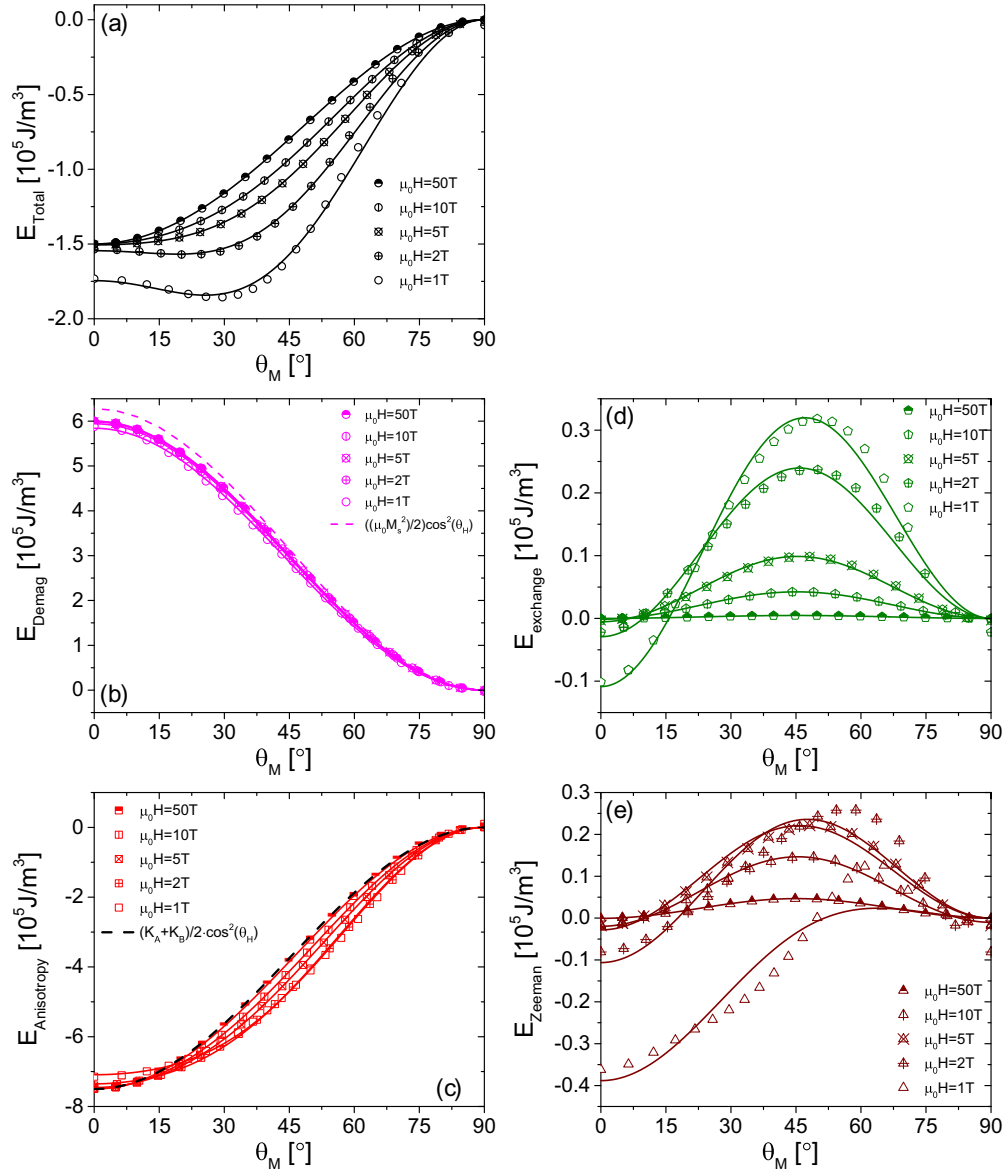


FIG. 2. Dependence of (a) the total energy density, (b) the demagnetizing energy density, (c) the anisotropy energy, (d) the exchange energy density, and (e) the Zeeman energy density on the average magnetization angle θ_M obtained after relaxing the magnetization with the indicated external magnetic field applied at different angles. The solid lines are a fit using the macrospin model, see Eq. (3). The dashed lines in (b) and (c) represent the expected angular dependence for the demagnetizing energy density of an infinite thin film and the volume averaged anisotropy energy density, respectively.

the magnetization for a perpendicular second-order anisotropy in regions A of $K_{2,A} = -1.5 \times 10^6 \text{ J/m}^3$ and a second-order anisotropy in regions B of $K_{2,B} = 0 \text{ J/m}^3$. For these simulations, the applied magnetic field was varied from $\mu_0 H = 1$ to 50 T.

As can be seen in Fig. 2(a) for applied fields less than 2 T the total energy density of the system has maxima along the out-of-plane ($\theta_M = 0^\circ$) and the in-plane ($\theta_M = 90^\circ$) orientations of the magnetization and a minimum at an intermediate angle. This is a clear indication that a higher-order anisotropy term will be required to describe this system using a macrospin approximation, although the microscopic model did not include such a term. Furthermore, this canted state of the magnetization, also known as easy-cone state [30], requires

that the second and fourth-order anisotropy term have opposite signs [31,32]. The solid lines in Fig. 2(a) show a fit to the simulation results using both a second-order and fourth-order anisotropy contribution:

$$E = E_0 + \tilde{K}_{2,\text{eff}} \cos^2 \theta_M + \frac{K_{4,\text{eff}}}{2} \cos^4 \theta_M, \quad (3)$$

where we use effective quantities to indicate a macrospin representation of the system. E_0 is an angle-independent offset. The effective anisotropy $\tilde{K}_{2,\text{eff}}$ in Eq. (3) contains both shape anisotropy and the uniaxial anisotropy contributions. In particular, for an infinite, homogeneously magnetized thin film, one could separate these two contributions as follows: $\tilde{K}_{2,\text{eff}} = \frac{\mu_0 M_s^2}{2} + K_{2,\text{eff}}$. However, in the case of lateral variations of

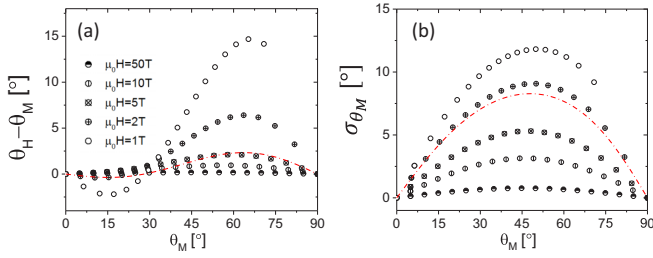


FIG. 3. (a) Deviation of the average angle of the magnetization θ_M from the angle of the applied field θ_H shown as a function of the average angle of the magnetization θ_M . The symbols represent the results from micromagnetic simulations with different strengths of the applied field. The red dash dotted line is the result obtained by ignoring exchange interaction and treating each region as a separate macrospin for an applied field $\mu_0 H = 5$ T. (b) Standard deviation σ_{θ_M} of the magnetization angle from its average orientation θ_M as a function of the same. The symbols represent the results from micromagnetic simulations with different strengths of the applied field. The red dash dotted line is the result obtained by ignoring exchange interaction and treating each region as a separate macrospin for an applied field $\mu_0 H = 5$ T, here the difference $\Delta\theta_M = \frac{\theta_B - \theta_A}{2}$ between the angle of the magnetization in region A and B is shown.

the microscopic second-order perpendicular anisotropy K_2 the film is not homogeneously magnetized [see Fig. 3(b)] and thus the shape anisotropy contribution to $\tilde{K}_{2,\text{eff}}$ is expected to be reduced from the value for an infinite film. This can be seen in Fig. 2(b), where E_{demag} , the energy contribution due to dipole-dipole interaction in the structure, is shown separately as a function of the average magnetization angle. For comparison, we also show the expectation for the angular dependence of this contribution for a homogeneously magnetized thin film ($\frac{\mu_0 M_s^2}{2} \cos^2 \theta_M$, dashed line). The main difference between the micromagnetic and the analytical result for a homogeneously magnetized thin film is indeed a small reduction of the amplitude of the second-order uniaxial anisotropy. However, we also observe that a fourth-order contribution is required to fit the angular dependence of the energy contribution of the dipole-dipole interaction using Eq. (3). With increasing external magnetic field, the magnetization in the structures becomes more homogenous [Fig. 3(b)] and thus the effective second-order uniaxial anisotropy approaches the thin film limit [see Fig. 4(a)] and the fourth-order anisotropy contribution diminishes [see Fig. 4(b)].

In Fig. 2(c), we show the anisotropy contribution to the total energy density of the system as a function of the magnetization angle. For comparison, the angular dependence of the anisotropy contribution of a homogeneously magnetized thin film with a second-order uniaxial anisotropy equal to the volume-averaged anisotropy of the two regions $\tilde{K}_{2,\text{eff}} = \frac{K_{2,A} + K_{2,B}}{2} = -0.75 \times 10^6 \text{ J/m}^3$ is also shown (dashed line). One notes that the energy difference between the out-of-plane easy axis and the in-plane hard axis is well approximated by the volume average $\tilde{K}_{2,\text{eff}}$. However, a significant fourth-order anisotropy $K_{4,\text{eff}}$ is required to fit this energy contribution using Eq. (3). Because the fourth-order contribution has the opposite sign compared to the second-order contribution, this causes the second-order anisotropy $\tilde{K}_{2,\text{eff}}$ extracted from the fit to be

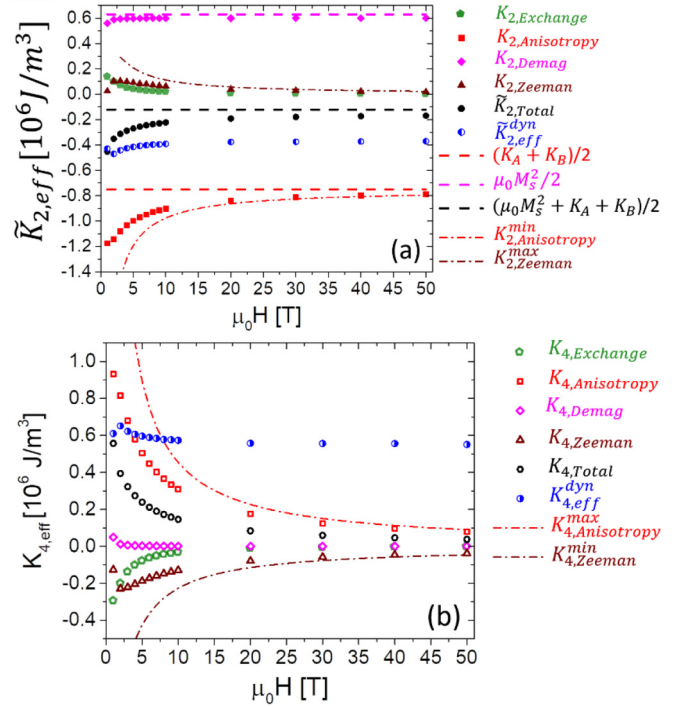


FIG. 4. (a) Field dependence of the effective second-order uniaxial anisotropy determined by fitting Eq. (3) to the angular dependence of the different contributions to the total energy, see Fig. 2. The dashed red line is the volume averaged second-order uniaxial anisotropy. The pink dashed line represents the demagnetization energy density for a homogeneously magnetized infinite film. The dash dotted red line is the anisotropy contribution to the effective second-order uniaxial anisotropy obtained by ignoring exchange interactions between the regions and treating them each as a macrospin. The dark red dash dotted line is the Zeeman contribution to the effective second-order anisotropy using the same simplified model. (b) Field dependence of the effective fourth-order uniaxial anisotropy. The dash dotted red lines represent contribution obtained by ignoring exchange interactions between the regions and treating them each as a macrospin, the anisotropy and Zeeman contribution are shown in red and dark red, respectively. The blue symbols in both graphs are the effective anisotropies determined from dynamical calculations, see Sec. III D.

smaller than the volume averaged anisotropy, i.e., $\tilde{K}_{2,\text{eff}} < \bar{K}_{2,\text{eff}}$. With increasing external applied field, the effective second-order anisotropy of this contribution approaches the volume average $\bar{K}_{2,\text{eff}}$ [see Fig. 4(a)], whereas the fourth-order contribution $K_{4,\text{eff}}$ approaches zero [see Fig. 4(b)]. Again, this is caused by the reduction of the inhomogeneity of the magnetization with increasing magnetic field [see Fig. 3(b)].

In Fig. 2(d), we show the exchange contribution to the total energy density of the system as a function of the magnetization angle. At high fields, this contribution closely follows the angular dependence of the inhomogeneity of the magnetization as shown in Fig. 3(b). However, at low fields, the average magnetization of the structure is not well aligned with the direction of the external magnetic field [see Fig. 3(a)] leading to a more complicated magnetization distribution and thus a more complex angular dependence of the exchange contribution. As shown in Fig. 2(d), this energy contribution can again be reasonably fitted using Eq. (3). The second-order uniaxial

anisotropy contribution due to exchange interaction is positive, while the fourth-order contribution is negative but comparable in magnitude. Both contributions diminish with increasing external magnetic field [see Figs. 4(a) and 4(b)].

Finally, in Fig. 2(e), the angular dependence of the Zeeman contribution to the total energy of the system is shown. The angular dependence of this energy contribution is mainly caused by the angular dependence of the deviation of the magnetization from the field direction [see Fig. 3(a)], while the inhomogeneity of the magnetization only plays a minor role. We would like to point out that even for a system with no lateral variations of the second-order uniaxial anisotropy, i.e., $K_{2,A} = K_{2,B}$, the system will show a similar angular dependence as the one in Fig. 2(e) for the Zeeman contribution to the total energy. This is because for finite external fields applied other than along the film normal ($\theta_H = 0^\circ$) or in the film plane ($\theta_H = 90^\circ$) the magnetization is never fully aligned with the field direction. The description of the angular dependence shown in Fig. 2(e) using Eq. (3) does not capture some of the more complex behavior at low fields caused by large changes and variations of the magnetization direction. However, the agreement of the fit using Eq. (3) significantly improves with increasing field. Like the exchange contribution, the Zeeman contribution leads to a positive second-order and a negative fourth-order uniaxial anisotropy contribution [see Figs. 4(a) and 4(b)]. The magnitude of both contributions is comparable to the exchange contributions. However, the Zeeman contribution to the fourth-order uniaxial anisotropy drops off slower with the applied field than the exchange contribution, see Fig. 4(b).

Figures 4(a) and 4(b) provide a visual summary of the results discussed in this section. Lateral variations of the second-order uniaxial anisotropy lead to the presence of a fourth-order uniaxial anisotropy, if one attempts to describe the system using a macrospin approximation. The main contributions to the total effective anisotropies are caused by the anisotropy contribution to the total energy. The total effective fourth-order anisotropy has the opposite sign as the total effective second-order anisotropy, which is a requirement for easy cone [33–35], which is often observed experimentally. The effective anisotropies show a complex field dependence that can be understood by considering all contributions to the energy of the system, as discussed in detail in this section. Also shown in Figs. 4(a) and 4(b) as dash-dotted lines [$K_{2,\text{Anisotropy}}^{\min}$ and $K_{2,\text{Zeeman}}^{\max}$ in (a) and $K_{4,\text{Anisotropy}}^{\max}$ and $K_{4,\text{Zeeman}}^{\min}$ in (b)] is the asymptotic behavior one expects by treating both regions separately as macrospins and ignoring exchange interaction. As can be seen in these figures, the micromagnetic results approach this asymptotic behavior for very large magnetic fields, well beyond what can typically be achieved experimentally. We note here that the curves for treating each region separately as a macrospin and ignoring exchange interaction are obtained by minimizing the free energy for region A and B separately, as if each region was an infinite thin film with anisotropy $K_{2,A}$ and $K_{2,B}$. The resulting deviation of the average angle of the magnetization $\theta_M = \frac{\theta_A + \theta_B}{2}$ from the external magnetic field direction and the difference $\Delta\theta_M = \frac{\theta_B - \theta_A}{2}$ between the angles in the two regions are shown exemplarily in Figs. 3(a) and 3(b), respectively, as red dash dotted lines for an external

magnetic field of $\mu_0 H = 5\text{T}$. This in turn enables to separately calculate the anisotropy energy and the Zeeman energy as a function of the magnetization angle θ_M and obtain the effective anisotropies $K_{2,\text{Anisotropy}}^{\min}$, $K_{2,\text{Zeeman}}^{\max}$, $K_{4,\text{Anisotropy}}^{\max}$, and $K_{4,\text{Zeeman}}^{\min}$ shown in Fig. 4, here the superscripts indicate that these values are an upper or lower limit for the corresponding fully micromagnetic calculations.

C. Influence of the length scale of lateral anisotropy variations on the quasistatic properties

So far, we have discussed the case of variations of the second-order uniaxial anisotropy for a fixed wavelength $L_x = L_y = 30\text{ nm}$. However, in physical samples one expects, for example, interfacial roughness to lead to variations of the second-order uniaxial anisotropy over a continuum of length scales. For the following discussion, we use the same simulation parameters as in the previous section, but now change the length scale of the lateral variations of the second-order uniaxial anisotropy by changing $L_x = L_y$.

In Figs. 5(a) and 5(b), we show the results of quasistatic simulations carried out in an external magnetic field $\mu_0 H = 5\text{ T}$. As discussed previously, the angular dependence of the individual energy contributions was fitted using the macrospin model description of Eq. (3). As expected for anisotropy fluctuations on short-length scales, the energy contribution due to dipole-dipole interaction leads to a significantly lower effective second-order uniaxial anisotropy $\bar{K}_{2,\text{eff}}$ contribution than one expects for a homogeneously magnetized film [dashed magenta line in Fig. 5(a)]. However, as the length scale of the anisotropy fluctuations increases, the effective second-order uniaxial anisotropy contribution due to dipole-dipole interaction approaches this value. As mentioned previously, the fourth-order uniaxial anisotropy contribution due to dipole-dipole interaction is small, given that the applied field is sufficiently large.

The anisotropy contribution to the effective second-order uniaxial anisotropy approaches the volume average $\bar{K}_{2,\text{eff}} = \frac{K_{2,A} + K_{2,B}}{2}$ [red dashed line in Fig. 5(a)] for anisotropy fluctuations over very short-length scales. This is expected, because in this case the exchange interaction dominates and forces the moments in neighboring regions to be parallel, thereby effectively averaging over them. The decrease of the effective second-order uniaxial anisotropy $\bar{K}_{2,\text{eff}}$ with increasing length scale of the anisotropy fluctuations is correlated with the increase of the fourth-order uniaxial anisotropy contribution. As discussed in the previous section, this fourth-order contribution is driven by the inhomogeneity of the magnetization, which vanishes along the in-plane and out-of-plane orientation of the applied field. However, for any other angle of the applied field, the magnetization varies spatially. With increasing length scale of the lateral anisotropy fluctuations, this inhomogeneity increases, as neighboring regions are less rigidly coupled, therefore leading to an increase of the effective fourth-order uniaxial anisotropy contribution. Furthermore, the energy difference between the in-plane and out-of-plane field orientations is always given by the volume average $\bar{K}_{2,\text{eff}}$, because in these two orientations the magnetization is homogenous and aligned along the magnetic field direction [see Figs. 3(a) and 3(b)]. Therefore, with increasing length scale of the

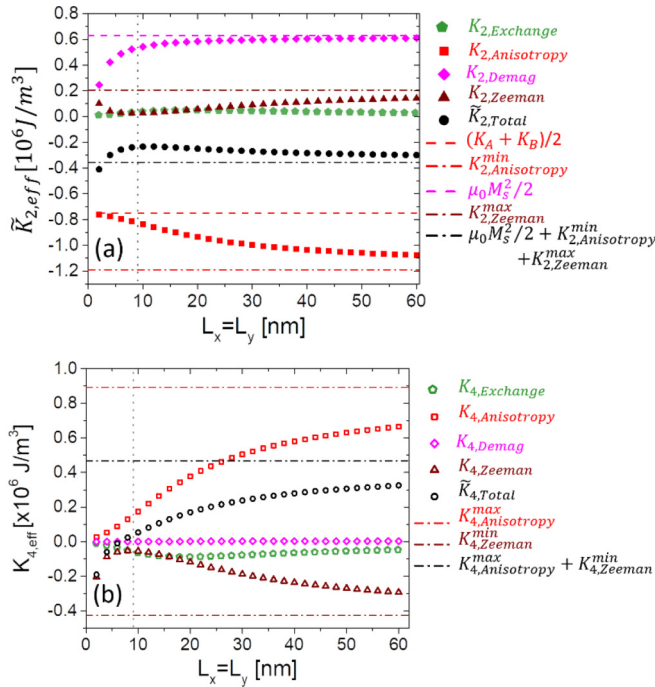


FIG. 5. (a) Dependence of the effective second-order uniaxial anisotropy on the lateral length scale of the second-order anisotropy variations. The dashed red line is the volume averaged second-order uniaxial anisotropy. The pink dashed line represents the demagnetization energy density for a homogeneously magnetized infinite film. The dash dotted red line is the anisotropy contribution to the effective second-order uniaxial anisotropy obtained by ignoring exchange interactions between the regions and treating them each as a macrospin. The dark red dash dotted line is the Zeeman contribution to the effective second-order anisotropy using the same simplified model. The black dash dotted line is the sum of demagnetization energy, the anisotropy and Zeeman contribution in the macrospin approximation. (b) Dependence of the effective fourth-order uniaxial anisotropy on the lateral length scale of the second-order anisotropy variations. The dash dotted red lines represent contributions obtained by ignoring exchange interactions between the regions and treating them each as a macrospin, the anisotropy and Zeeman contribution are shown in red and dark red, respectively. The black dash dotted line is the sum of these contributions. The gray vertical dashed lined is the length scale λ_{eff} , see text for details.

anisotropy fluctuations, the effective second-order uniaxial anisotropy decreases as the fourth-order uniaxial anisotropy increases. Both effective anisotropies extracted from the full micromagnetic model approach the values expected based on treating the individual regions as macrospins and ignoring the exchange interaction. See the dash-dotted lines for $K_{2,\text{Anisotropy}}^{\text{min}}$ in Fig. 5(a) and for $K_{4,\text{Anisotropy}}^{\text{max}}$ in Fig. 5(b).

Due to the large applied magnetic field, the contribution of the exchange interaction to both the effective second-order and fourth-order uniaxial anisotropy remains relatively small over the entire range of the length scales investigated. For very short-length scales of the lateral anisotropy fluctuations the contributions are small because neighboring regions are rigidly coupled to each other. For very large-length scales on the other hand the contributions due to the exchange interaction diminish because the individual regions are homogeneously

magnetized and only the boundaries between them lead to an angle-dependent exchange interaction contribution to the total energy of the system. At intermediate-length scales, this leads to a maximum for the effective second-order uniaxial anisotropy [Fig. 5(a)] and to a minimum for the effective fourth-order uniaxial anisotropy [Fig. 5(b)].

On the other hand, the large applied magnetic field combined with the deviation of the magnetization direction from the applied field direction, as discussed in the previous section, also leads to an angular dependence of the Zeeman contribution to the energy of the system. With increasing length scale of the lateral anisotropy variations, the effective second- and fourth-order anisotropies of the full micromagnetic model approach the values expected based on treating the individual regions as macrospins and ignoring the exchange interaction, see the dash-dotted lines for $K_{2,\text{Zeeman}}^{\text{max}}$ in Fig. 5(a) and for $K_{4,\text{Zeeman}}^{\text{min}}$ in Fig. 5(b).

In summary, the total effective fourth-order anisotropy caused by large-scale lateral variations of the second-order anisotropy has two main contributions: from the Zeeman and the anisotropy contribution to the total energy of the system. As can be seen in Fig. 5(b), these two contributions have opposite signs. For lateral variations, over shorter length scales the exchange interaction also contributes significantly to the total effective fourth-order anisotropy of the system. Furthermore, in this case, the contribution of the dipole-dipole interaction to the effective second-order anisotropy deviates significantly from the thin film limit and thus needs to be taken into account. Finally, we can compare the variations seen in Fig. 5 with characteristic length scales of the system. For the system discussed here, the demagnetizing energy results in a characteristic length of $\lambda_d = \sqrt{2A/(\mu_0 M_s^2)} \approx 4$ nm, while the characteristic length associated with the uniaxial anisotropy in regions A with a second-order uniaxial anisotropy $K_{2,A} = -1.5 \times 10^6$ J/m³ is $\lambda_A = \sqrt{A/|K_{2,A}|} \approx 3$ nm [36]. However, for a system comprised of regions A and B with different second-order uniaxial anisotropies one can expect the length scale $\lambda_{\text{eff}} = \sqrt{A/|\frac{\mu_0 M_s^2}{2} + \bar{K}_{2,\text{eff}}|} \approx 9$ nm, associated with the sum of shape anisotropy and volume averaged anisotropy to play a more important role [36]. This length scale is shown as a gray vertical dashed line in Fig. 5 and can indeed be considered a characteristic length scale of the system.

D. Dynamic properties

To probe the dynamical response of the system, a static magnetic field \vec{H} is applied either along the film normal ($\vec{H} = H \cdot \hat{z}$) or in the film plane ($\vec{H} = H \cdot \hat{y}$). Initially, the system is relaxed in the presence of an additional small field \vec{h}_p perpendicular to the static magnetic field, i.e., $\vec{H}_{\text{total}} = \vec{H} + \vec{h}_p$ (see Fig. 6). At $t = 0$, the small perpendicular field is removed and the time evolution of the relaxation of the magnetization is recorded. The time evolution of the magnetization in each cell of the micromagnetic model is described by the Landau-Lifshitz-Gilbert equation of motion [29,37–39]:

$$\frac{d\vec{M}}{dt} = -\gamma \vec{M} \times \vec{H}_{\text{eff}} + \frac{1}{M_s} \vec{M} \times \alpha \frac{d\vec{M}}{dt}, \quad (4)$$

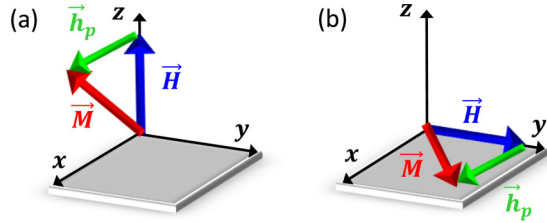


FIG. 6. Sketch of the configuration for determining the dynamic properties of the system. In (a), the out-of-plane configuration and in (b) the in-plane configuration are shown. The small additional field \vec{h}_p is only present during relaxation of the initial state and is removed at $t = 0$.

where \vec{M} is the magnetization vector, M_S is the saturation magnetization, γ is the gyromagnetic ratio, and α is the damping parameter. For the simulations discussed below, we used $\gamma = 2.21 \times 10^5 \text{ m A}^{-1} \text{ s}^{-1}$ and $\alpha = 0.007$. The effective field H_{eff} entering the Landau-Lifshitz-Gilbert equation of motion includes the external magnetic field, dipole field, anisotropy field and exchange field. In Fig. 7(a), an example of the resulting time evolution of the average magnetization is shown when the external magnetic field ($\mu_0 H = 2 \text{ T}$) is applied along the film normal. To enable a quantitative analysis of the time dependence of all cells in the simulation volume, we calculate the power spectral density for each cell and calculate the average power spectral density [19,40], as shown in Fig. 7(b). The resulting spectrum reveals a number of resonant features that correspond to the fundamental resonance mode and higher order lateral standing spin wave modes in the structure. By plotting the contribution of each cell to the average power spectral density at the different resonance frequencies, one can visualize the mode profiles [see power spectral density maps shown as insets of Fig. 7(b)].

For the fundamental mode in the out-of-plane configuration one notes that regions B with $K_{2,B} = 0 \text{ J/m}^3$ contribute significantly more to the power spectral density. In other

words, the resonance is preferably localized in region B. In Fig. 8, the dependence of this localization on the lateral length scale of the anisotropy variations is quantified by plotting the ratio of the power spectral density contribution P_A of region A to the total power spectral density P_{total} . As expected in the limit of vanishing small length scales both regions contribute equally to the resonance, due to the strong exchange coupling between neighboring regions effectively averaging out the variations. As discussed above, when the static magnetic field is applied perpendicular to the film plane with increasing length scale of the lateral anisotropy variation the resonance becomes increasingly localized in region B, as expected [41]. However, in the in-plane case, the situation is reversed, i.e., here with increasing length scale the resonance becomes increasingly localized in region A. In both cases, the resonance is localized in the region of the structure with the lower excitation energy, as can be expected. Correspondingly, this increased localization with increasing length scale of the lateral anisotropy variations causes the resonance frequency to approach the resonance frequency f_B of a film with an anisotropy $K_{2,B}$ in the out-of-plane case, whereas in the same limit the resonance frequency in the in-plane case approaches the resonance frequency f_A of a film with an anisotropy $K_{2,A}$. This has important consequences for the effective anisotropies that one extracts from the dynamical data. The Kittel equations for systems with a second- and fourth-order perpendicular anisotropy are given by [33,42]

$$f_{\perp} = \gamma' (H - M_{\text{eff},\perp}), \quad (5a)$$

$$f_{\parallel} = \gamma' \sqrt{H(H + M_{\text{eff},\parallel})}, \quad (5b)$$

with $\gamma' = \gamma/2\pi$ and the effective out-of-plane and in-plane magnetizations given by

$$M_{\text{eff},\perp} = \frac{2\tilde{K}_{2,\text{eff}}^{\text{dyn}}}{\mu_0 M_S} + \frac{K_{4,\text{eff}}^{\text{dyn}}}{\mu_0 M_S} \quad (6a)$$

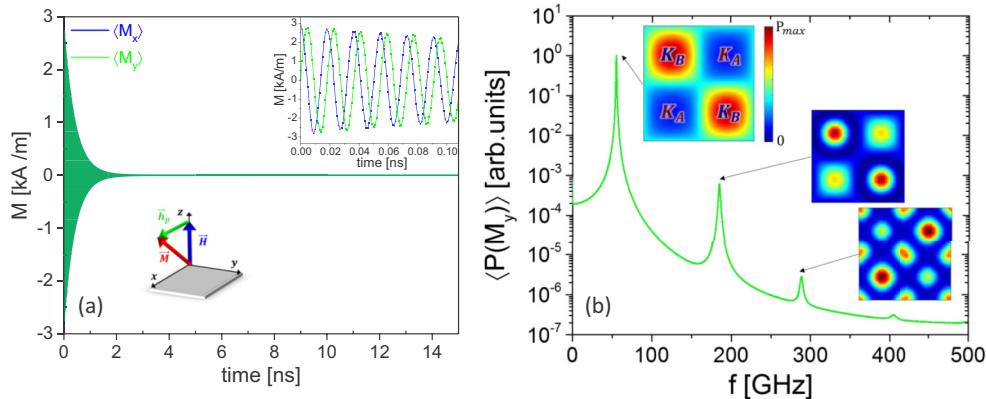


FIG. 7. (a) Time evolution of the average magnetization components M_x and M_y for a $20 \text{ nm} \times 20 \text{ nm}$ structure with $K_{2,A} = -1.5 \times 10^{-6} \text{ J/m}^3$ and $K_B = 0 \text{ J/m}^3$ with an external magnetic field of $\mu_0 H = 2 \text{ T}$ applied along the film normal $\theta_H = 0^\circ$. A small additional field $h_p = 0.006 \text{ T}$ along the x axis was removed at $t = 0$. The inset shows the time evolution during the first tenth of a nanosecond. (b) Shows $P(M_y)$, i.e., the power spectral density of the y component of the magnetization averaged over all cells in the simulation volume for the same parameters as in (a). The insets of this figure show the power spectral density maps for the first three resonances at frequencies $f_{\perp 1} = 54.9 \text{ GHz}$ (fundamental resonance mode), $f_{\perp 2} = 184 \text{ GHz}$, and $f_{\perp 3} = 288 \text{ GHz}$. Here the color indicates the contribution of each cell to the power spectral density, with dark red indicating the largest and dark blue zero contribution.

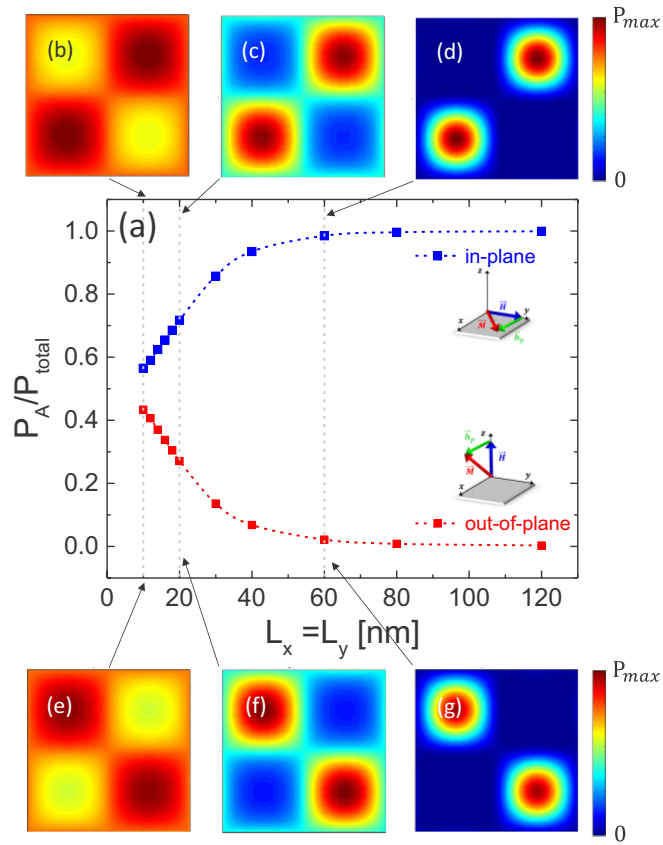


FIG. 8. (a) Dependence of the contribution of region A to the total power spectral density of the fundamental mode on the lateral length scale $L_{x,y}$ of the variations of the anisotropy. (b)–(d) show spectral maps with the static field applied in-plane whereas (e)–(g) show spectral maps with the static field applied out-of-plane. For (b) and (e) $L_x = L_y = 10$ nm, for (c) and (f) $L_x = L_y = 20$ nm, and for (d) and (g) $L_x = L_y = 60$ nm.

and

$$M_{\text{eff},\parallel} = \frac{2\tilde{K}_{2,\text{eff}}^{\text{dyn}}}{\mu_0 M_S}, \quad (6b)$$

respectively. From the numerical simulations, one can therefore extract the dynamic effective second-order uniaxial anisotropy $\tilde{K}_{2,\text{eff}}^{\text{dyn}}$ and effective fourth-order uniaxial anisotropy $K_{4,\text{eff}}^{\text{dyn}}$ that describe the dynamical data in a macrospin approximation (see blue data points in Fig. 9). The definitions of $\tilde{K}_{2,\text{eff}}^{\text{dyn}}$ and $K_{4,\text{eff}}^{\text{dyn}}$ are the same as those of $\tilde{K}_{2,\text{eff}}$ and $K_{4,\text{eff}}$, the additional superscript indicating that these quantities are determined from the magnetization dynamics of the system. For comparison, the results from quasistatic calculations at the same external magnetic field [similar to Figs. 5(a) and 5(b)] are also included in Fig. 9 (black data points). The limiting cases for the quantities determined from dynamical simulations can be understood as follows. For lateral anisotropy variations at vanishingly small length scales, i.e., $L_{x,y} \rightarrow 0$, the exchange coupling will effectively average out these variations and thus the effective second-order uniaxial anisotropy will approach the volume average of the two anisotropies $\tilde{K}_{2,\text{eff}}$. In this limit, the resonance has equal contributions from regions A and B for

both the in-plane and out-of-plane configurations. Therefore the effective magnetizations for both configurations will be equal and thus $K_{4,\text{eff}}^{\text{dyn}}$ vanishes for $L_{x,y} \rightarrow 0$ [see Fig. 9(b)]. For lateral anisotropy variations, over very large-length scales, i.e., $L_{x,y} \rightarrow \infty$, the resonance in the out-of-plane configuration will become localized in region B whereas the resonance in the in-plane configuration will become localized in region A. Therefore

$$f_{\perp} \xrightarrow{L_{x,y} \rightarrow \infty} f_B \quad (7a)$$

and

$$f_{\parallel} \xrightarrow{L_{x,y} \rightarrow \infty} f_A \quad (7b)$$

And, consequently,

$$\tilde{K}_{2,\text{eff}}^{\text{dyn}} \xrightarrow{L_{x,y} \rightarrow \infty} \frac{\mu_0 M_S^2}{2} + K_{2,A} \quad (8a)$$

and

$$K_{4,\text{eff}}^{\text{dyn}} \xrightarrow{L_{x,y} \rightarrow \infty} K_{2,B} - K_{2,A}. \quad (8b)$$

As can be seen in Figs. 9(a) and 9(b), our simulation results for the dynamic higher-order anisotropies approach these predicted values (blue dashed lines) for large length scales. However, the length scale dependence of the effective anisotropies obtained from the dynamic response of the system is significantly different from those obtained from quasistatic calculations for the same applied field. As these differences persist over the entire range of length scales of the anisotropy variations, including the asymptotic behavior at short and large length scales, we also expect a difference between the anisotropies obtained from quasistatic and dynamic measurements for physical samples. For those, interface roughness will lead to a continuous distribution of the second-order uniaxial anisotropy and the relevant length scales will be determined by the type of interface morphology present in the samples and its characteristic parameters [43]. The dynamic response of the system also shows a markedly different field dependence of the effective anisotropies when compared to the quasistatic results (see Fig. 4). While the effective anisotropies are weakly dependent on the external applied field through its influence on the equilibrium configuration of the magnetization the amount of localization has a much stronger influence. This is particularly evident for the dynamic fourth-order effective anisotropy, which remains at a finite positive value even for the largest fields used in Fig. 4(b), whereas the quasistatic results approach zero in this limit. We would like to point out that recent experimental observations of a field dependence of the second-order effective anisotropy [25] appear to be consistent with the predicted sensitivity of the effective anisotropies to the equilibrium configuration at low fields. Clearly, more systematic experimental work is needed to verify whether spatial variations of the second-order anisotropy are indeed responsible for these observations.

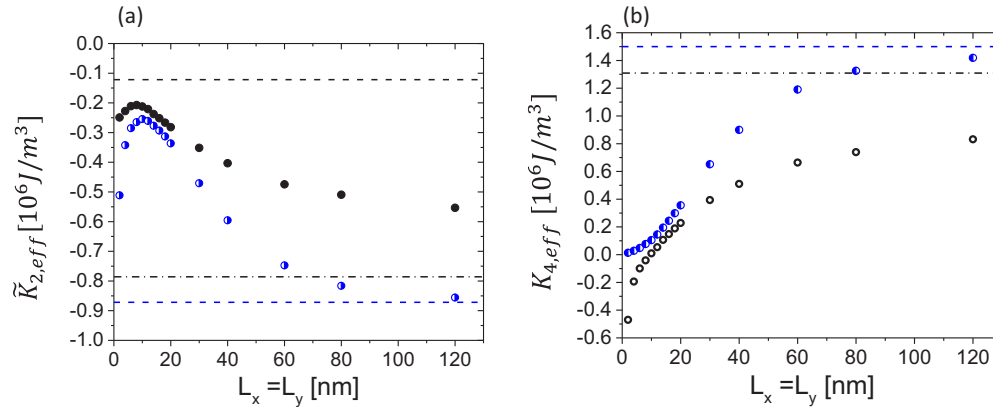


FIG. 9. Effective second-order uniaxial anisotropy as a function of the lateral length scale $L_{x,y}$ of the variations of the anisotropy. The anisotropy $\tilde{K}_{2,\text{eff}}^{\text{dyn}}$ for the dynamic simulations is shown as blue symbols whereas the anisotropy $\tilde{K}_{2,\text{eff}}$ determined from quasistatic simulations is shown as black symbols. The dashed black line shows the thin film limit with an average anisotropy, i.e., $\frac{\mu_0 M_s^2}{2} + \frac{K_{2,A} + K_{2,B}}{2}$. The dashed blue line represents the large-length scale limit for the dynamical simulations $\frac{\mu_0 M_s^2}{2} + K_{2,A}$. (b) Effective fourth-order uniaxial anisotropy as a function of the lateral length scale $L_{x,y}$ of the variations of the anisotropy. The anisotropy $K_{4,\text{eff}}^{\text{dyn}}$ for the dynamic simulations is shown as blue symbols whereas the anisotropy $K_{4,\text{eff}}$ determined from quasistatic simulations is shown as black symbols. The dashed blue line represents the large-length scale limit for the dynamical simulations $K_{2,B} - K_{2,A}$. In both figures, the dash dotted black lines are the limiting values expected for the quasistatic effective anisotropies, obtained by treating each region as a macrospin and ignoring exchange interaction, see Sec. IIC.

III. SUMMARY AND DISCUSSION

In summary, we have analyzed how lateral variations of a second-order uniaxial anisotropy affect the effective anisotropies required to describe the system in the framework of a macrospin model. For the quasistatic and dynamic calculations discussed in this manuscript, we find that second-order and fourth-order effective anisotropies are sufficient to capture the main properties of the system in the macrospin model. For the quasistatic properties, we find that the effective fourth-order uniaxial anisotropy is closely linked to deviations of the average magnetization angle from the field direction and the lateral variation of the magnetization direction in the structure. This results in a strong field dependence of the effective anisotropies. The dependence of the effective anisotropies on the lateral length scale of the variations of the second-order uniaxial anisotropy are profoundly different for the quasistatic and dynamic calculations. The underlying reason for this difference is that the quasistatic properties are averaged over the entire sample volume whereas the observable dynamic properties depend sensitively on the degree of localization of the resonance. This localization depends not only on the lateral length scale of the anisotropy variations, but also on the field orientation. While there have also been some

reports on the differences between anisotropies determined using quasistatic and dynamic methods [44–46], more experimental work is needed to clarify this aspect, particularly, for systems with perpendicular anisotropy. Interpretation of experimental results for systems where lateral variations of the second-order anisotropy are caused by interfacial roughness will be complicated by the continuous distribution of anisotropies in the system. Thus, in order to make a quantitative comparison, a careful characterization of the interfacial roughness will be required [43,47]. However, we would like to point out that a continuous distribution of the second-order anisotropy is expected to result in a significant inhomogeneous broadening of the resonance that increases with the distribution of the anisotropy fields [41], very much in line with what has recently been reported for CoFe/Ni multilayers [48].

ACKNOWLEDGMENTS

This work was supported by National Science Foundation Faculty Early Career Development Program (NSF-CAREER) Grants No. 0952929 and No. 1452670. We would also like to acknowledge the support of the University of Alabama High Performance Computing facilities and staff.

- [1] S. Mangin, Y. Henry, D. Ravelosona, J. A. Katine, and E. E. Fullerton, Reducing the critical current for spin-transfer switching of perpendicularly magnetized nanomagnets, *Appl. Phys. Lett.* **94**, 012502 (2009).
- [2] E. Chen, D. Apalkov, A. Driskill-Smith, A. Khvalkovskiy, D. Lottis, K. Moon, V. Nikitin, A. Ong, X. Tang, S. Watts, R. Kawakami, M. Krounbi, S. A. Wolf, S. J. Poon, J. W. Lu, A. W. Ghosh, M. Stan, W. Butler, T. Mewes, S. Gupta, C. K. A. Mewes, P. B. Visscher, and R. A. Lukaszew, Progress and prospects of spin transfer torque random access memory, *IEEE Trans. Magn.* **48**, 3025 (2012).
- [3] D. Weller, Y. Wu, J. Stöhr, M. G. Samant, B. D. Hermsmeier, and C. Chappert, Orbital magnetic moments of Co in multilayers with perpendicular magnetic anisotropy, *Phys. Rev. B* **49**, 12888 (1994).
- [4] J. M. Beaujour, D. Ravelosona, I. Tudosa, E. E. Fullerton, and A. D. Kent, Ferromagnetic resonance linewidth in ultrathin films with perpendicular magnetic anisotropy, *Phys. Rev. B* **80**, 180415 (2009).
- [5] J. Zhu, J. A. Katine, G. E. Rowlands, Y.-J. Chen, Z. Duan, J. G. Alzate, P. Upadhyaya, J. Langer, P. K. Amiri, K. L. Wang, and I. N. Krivorotov, Voltage-Induced Ferromagnetic Resonance

- in Magnetic Tunnel Junctions, *Phys. Rev. Lett.* **108**, 197203 (2012).
- [6] A. Koziol-Rachwał, W. Skowroński, T. Ślęzak, D. Wilgocka-Ślęzak, J. Przewoźnik, T. Stobiecki, Q. H. Qin, S. v. Dijken, and J. Korecki, Room-temperature perpendicular magnetic anisotropy of MgO/Fe/MgO ultrathin films, *J. Appl. Phys.* **114**, 224307 (2013).
- [7] K. Makoto, I. Hiroshi, T. Tomohiro, Y. Kay, K. Hitoshi, F. Akio, A. Koji, and Y. Shinji, Effect of MgO cap layer on Gilbert damping of FeB electrode layer in MgO-based magnetic tunnel junctions, *Appl. Phys. Express* **6**, 073002 (2013).
- [8] P. Bruno, Tight-binding approach to the orbital magnetic moment and magnetocrystalline anisotropy of transition-metal monolayers, *Phys. Rev. B* **39**, 865 (1989).
- [9] S. Ayaz Khan, P. Blaha, H. Ebert, J. Minár, and O. Šipr, Magnetocrystalline anisotropy of FePt: A detailed view, *Phys. Rev. B* **94**, 144436 (2016).
- [10] A. Fert and P. M. Levy, Role of Anisotropic Exchange Interactions in Determining the Properties of Spin-Glasses, *Phys. Rev. Lett.* **44**, 1538 (1980).
- [11] P. M. Levy and A. Fert, Anisotropy induced by nonmagnetic impurities in Cu Mn spin-glass alloys, *Phys. Rev. B* **23**, 4667 (1981).
- [12] L. Rózsa, U. Atxitia, and U. Nowak, Temperature scaling of the Dzyaloshinsky-Moriya interaction in the spin wave spectrum, *Phys. Rev. B* **96**, 094436 (2017).
- [13] B. Heinrich, T. Monchesky, and R. Urban, Role of interfaces in higher order angular terms of magnetic anisotropies: Ultrathin film structures, *J. Magn. Magn. Mater.* **236**, 339 (2001).
- [14] F. Porrati, W. Wulfhekel, and J. Kirschner, An analytical model for ultrathin films with spatially varying magnetic anisotropies, *J. Magn. Magn. Mater.* **270**, 22 (2004).
- [15] J. Miltat, G. Albuquerque, and A. Thiaville, in *Spin Dynamics in Confined Magnetic Structures I*, edited by B. Hillebrands and K. Ounadjela (Springer, Berlin, Heidelberg, 2002), p. 1.
- [16] J. E. Miltat and M. J. Donahue, in *Handbook of Magnetism and Advanced Magnetic Materials* (Wiley, New York, 2007), Vol. 2, pp. 742–764.
- [17] D. V. Berkov, K. Ramstöck, and A. Hubert, Solving micromagnetic problems. Towards an optimal numerical method, *Phys. Status Solidi A* **137**, 207 (1993).
- [18] F. Josef and S. Thomas, Micromagnetic modelling - the current state of the art, *J. Phys. D: Appl. Phys.* **33**, R135 (2000).
- [19] D. Kumar and A. O. Adeyeye, Techniques in micromagnetic simulation and analysis, *J. Phys. D: Appl. Phys.* **50**, 343001 (2017).
- [20] J. Xiao, A. Zangwill, and M. D. Stiles, Macrospin models of spin transfer dynamics, *Phys. Rev. B* **72**, 014446 (2005).
- [21] W. H. Butler, T. Mewes, C. K. A. Mewes, P. B. Visscher, W. H. Rippard, S. E. Russek, and R. Heindl, Switching distributions for perpendicular spin-torque devices within the macrospin approximation, *IEEE Trans. Magn.* **48**, 4684 (2012).
- [22] K. D. Usadel, Temperature-dependent dynamical behavior of nanoparticles as probed by ferromagnetic resonance using Landau-Lifshitz-Gilbert dynamics in a classical spin model, *Phys. Rev. B* **73**, 212405 (2006).
- [23] D. A. Garanin and H. Kachkachi, Surface Contribution to the Anisotropy of Magnetic Nanoparticles, *Phys. Rev. Lett.* **90**, 065504 (2003).
- [24] R. Yanes, O. Chubykalo-Fesenko, H. Kachkachi, D. A. Garanin, R. Evans, and R. W. Chantrell, Effective anisotropies and energy barriers of magnetic nanoparticles with Néel surface anisotropy, *Phys. Rev. B* **76**, 064416 (2007).
- [25] I. Barsukov, Y. Fu, A. M. Gonçalves, M. Spasova, M. Farle, L. C. Sampaio, R. E. Arias, and I. N. Krivorotov, Field-dependent perpendicular magnetic anisotropy in CoFeB thin films, *Appl. Phys. Lett.* **105**, 152403 (2014).
- [26] <http://magneticslab.ua.edu/micromagnetics-code.html>.
- [27] A. J. Newell, W. Williams, and D. J. Dunlop, A generalization of the demagnetizing tensor for nonuniform magnetization, *J. Geophys. Res.: Solid Earth* **98**, 9551 (1993).
- [28] M. J. Donahue and D. G. Porter, Exchange energy formulations for 3D micromagnetics, *Physica B: Condens. Matter* **343**, 177 (2004).
- [29] A. Aharoni, in *Introduction to the Theory of Ferromagnetism*, 2nd ed. (Oxford University Press, Oxford, 2001), p. 174.
- [30] G. Asti and F. Bolzoni, Theory of first order magnetization processes: Uniaxial anisotropy, *J. Magn. Magn. Mater.* **20**, 29 (1980).
- [31] Y. Millev and M. Fähnle, Types of temperature dependence of single-ion magnetic anisotropy constants by general thermodynamic considerations, *Phys. Rev. B* **52**, 4336 (1995).
- [32] Y. T. Millev, H. P. Oepen, and J. Kirschner, Influence of external field on spin reorientation transitions in uniaxial ferromagnets. I. General analysis for bulk and thin-film systems, *Phys. Rev. B* **57**, 5837 (1998).
- [33] J. M. Shaw, H. T. Nembach, M. Weiler, T. J. Silva, M. Schoen, J. Z. Sun, and D. C. Worledge, Perpendicular magnetic anisotropy and easy cone state in Ta/Co₆₀Fe₂₀B₂₀/MgO, *IEEE Magn. Lett.* **6**, 1 (2015).
- [34] K. A. Seu, S. Roy, J. J. Turner, S. Park, C. M. Falco, and S. D. Kevan, Cone phase and magnetization fluctuations in Au/Co/Au thin films near the spin-reorientation transition, *Phys. Rev. B* **82**, 012404 (2010).
- [35] R. L. Stamps, L. Louail, M. Hehn, M. Gester, and K. Ounadjela, Anisotropies, cone states, and stripe domains in Co/Pt multilayers, *J. Appl. Phys.* **81**, 4751 (1997).
- [36] A. H. a. R. Schäfer, *Magnetic Domains* (Springer-Verlag, Berlin, Heidelberg, 1998).
- [37] T. L. Gilbert, *Phys. Rev.* **100**, 1243 (1955). [Abstract only; full report, Armor Research Foundation Project No. A059, Supplementary Report, May 1, 1956] (unpublished).
- [38] T. L. Gilbert, A phenomenological theory of damping in ferromagnetic materials, *IEEE Trans. Magn.* **40**, 3443 (2004).
- [39] C. Mewes and T. Mewes, in *Handbook of Nanomagnetism* (Pan Stanford, Singapore, 2015), p. 71.
- [40] R. D. McMichael and M. D. Stiles, Magnetic normal modes of nanoelements, *J. Appl. Phys.* **97**, 10J901 (2005).
- [41] R. D. McMichael, D. J. Twisselmann, and A. Kunz, Localized Ferromagnetic Resonance in Inhomogeneous Thin Films, *Phys. Rev. Lett.* **90**, 227601 (2003).
- [42] Z. R. Tadisina, A. Natarajarathinam, B. D. Clark, A. L. Highsmith, T. Mewes, S. Gupta, E. Chen, and S. Wang, Perpendicular magnetic tunnel junctions using Co-based multilayers, *J. Appl. Phys.* **107**, 09C703 (2010).
- [43] Y. P. Zhao, G. Palasantzas, G. C. Wang, and J. T. M. De Hosson, Surface/interface-roughness-induced demagnetizing effect in thin magnetic films, *Phys. Rev. B* **60**, 1216 (1999).

- [44] R. Lopusnik, J. P. Nibarger, T. J. Silva, and Z. Celinski, Different dynamic and static magnetic anisotropy in thin PermalloyTM films, *Appl. Phys. Lett.* **83**, 96 (2003).
- [45] M. L. Schneider, A. B. Kos, and T. J. Silva, Dynamic anisotropy of thin Permalloy films measured by use of angle-resolved pulsed inductive microwave magnetometry, *Appl. Phys. Lett.* **86**, 202503 (2005).
- [46] D. Xue and X. Fan, Comment on “Dynamic anisotropy of thin Permalloy films measured by use of angle-resolved pulsed inductive microwave magnetometry” [*Appl. Phys. Lett.* 86, 202503 (2005)], *Appl. Phys. Lett.* **90**, 116101 (2007).
- [47] T. Mewes, M. Rickart, A. Mougin, S. O. Demokritov, J. Fassbender, B. Hillebrands, and M. Scheib, Comparative study of the epitaxial growth of Cu on MgO(001) and on hydrogen terminated Si(001), *Surf. Sci.* **481**, 87 (2001).
- [48] J. M. Shaw, H. T. Nembach, and T. J. Silva, Resolving the controversy of a possible relationship between perpendicular magnetic anisotropy and the magnetic damping parameter, *Appl. Phys. Lett.* **105**, 062406 (2014).